NEUROSCIENCE

A twisted visual field map in the primate dorsomedial cortex predicted by topographic continuity

Hsin-Hao Yu[1,2,3]*, Declan P. Rowley[1,2], Nicholas S. C. Price[1,2], Marcello G. P. Rosa[1,2]*, Elizabeth Zavitz[1,2]*

Adjacent neurons in visual cortex have overlapping receptive fields within and across area boundaries, an arrangement theorized to minimize wiring cost. This constraint is traditionally thought to create retinotopic maps of opposing field signs (mirror and nonmirror visual field representations) in adjacent areas, a concept that has become central in current attempts to subdivide the extrastriate cortex. We simulated the formation of retinotopic maps using a model that balances constraints imposed by smoothness in the representation within an area and by congruence between areas. As in the primate cortex, this model usually leads to alternating mirror and nonmirror maps. However, we found that it can also produce a more complex type of map, consisting of sectors with opposing field sign within a single area. Using fully quantitative electrode array recordings, we then demonstrate that this type of inhomogeneous map exists in the controversial dorsomedial region of the primate extrastriate cortex.

INTRODUCTION

Sensory cortices represent the world in mosaics of topographically organized maps of the receptor surfaces. In the visual cortex, neurons in adjacent columns have receptive fields that represent overlapping regions of the retina, both within and across area boundaries. This characteristic of topographic continuity is believed to be derived from a strong developmental constraint for minimizing the wiring cost of the underlying local circuits, largely represented by intrinsic connections (*1*, *2*). In early visual cortex, topographic continuity is theorized to result in areas being organized as alternating bands that form mirror and nonmirror representations of the visual field (Fig. 1A) (*3*, *4*). "Field sign," a metric that indicates whether the local structure of a map forms part of a mirror or nonmirror representation of the visual field (*5*), can be used to determine the transition between the first and second visual areas (V1 and V2) and the extent of these areas (*6*). Field sign has become extensively used as a criterion to parse areas in functional mapping studies using both functional magnetic resonance imaging and electrophysiology (*5*–*10*).

The use of field sign as the main criterion for identifying areal boundaries is based on the assumption that an alternating field sign organization, analogous to that characterizing the V1/V2 region, extends throughout the visual cortex. However, the possibility that topographic continuity could allow more complicated maps to form has not been fully investigated with computational models. For example, in primates, V2 adjoins a mosaic of smaller areas, each occupying a specific sector of its rostral border (*4*, *5*, *9*–*11*). This configuration differs substantially from the concentric organization of V1 and V2, and it is unclear if, in this situation, pairs of adjacent areas are expected to consistently have opposing field signs. In addition, experimental observations show that neurons on either side of a border between areas represent the same region of the visual field, suggesting that the maximization of topographic continuity within a map (i.e., smoothness) is constrained by topographic continuity with neighboring maps (i.e., congruence). Given that visual areas develop asynchronously (*4*, *12*–*14*), the constraints imposed by topographic continuity within an area and across area borders might have different strengths, depending on the developmental schedules of the surrounding cortex. Presently, it is unclear whether empirical mapping data are consistent with models based on the interactions between these factors.

In a traditional view, each visual area is thought to form a complete and systematic map of the visual field (*15*). However, frequent reports of fractured and incomplete maps (*16*) have come to suggest that the idealized view of homogeneous field sign within an area, or even topographic continuity itself, might be violated in extrastriate areas. Here, we present a computational model of the formation of extrastriate maps, constrained by smoothness within an area, and congruence across area boundaries. This model predicts that, under certain conditions, topographical maps with two surprising features can emerge: first, a "twist" in visual field topography, leading to sectors of mirror and nonmirror representation within a single area, and second, regions of rapid change in receptive field position within the map, which bridge the transition between mirror and nonmirror sectors. Using a quantitative method to map the controversial dorsomedial extrastriate region rostral to V2 (*11*, *17*) in the marmoset monkey in high resolution, we then demonstrate the existence of this type of map in the visual cortex. This combination of modeling and electrophysiological results establishes that, even under a simple model of map formation, the resulting topography of cortical maps can be complex. It also suggests that robust parcellation of the visual cortex requires a deeper understanding of the principles behind the formation of maps during development, as well as a more detailed analysis than that afforded by field sign alone.

RESULTS

The formation of extrastriate retinotopic maps can be modeled with continuity constraints

The upper and lower quadrants of the visual field are both represented in V1 and V2 as strips of nearly equal length, located in the

[1]Department of Physiology and Neuroscience Program Biomedicine Discovery Institute, Monash University, Clayton, Victoria, Australia. [2]ARC Centre of Excellence for Integrative Brain Function, Monash University, Clayton, Victoria, Australia. [3]IBM Research Australia, Southbank, VIC, Australia.
*Corresponding author. Email: hsin-hao.yu@au1.ibm.com (H.-H.Y.); marcello.rosa@monash.edu (M.G.P.R.); elizabeth.zavitz@monash.edu (E.Z.)

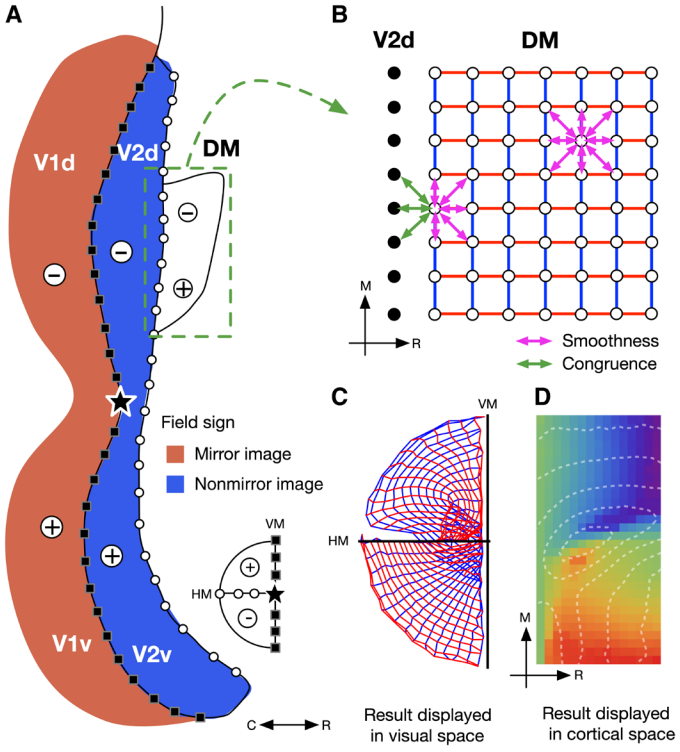

Fig. 1. A model for retinotopic map formation in the extrastriate cortex. (**A**) Schematic of early visual areas on flat-mounted cortex. The green rectangle represents the cortical region whose retinotopy was learned by the model (area "DM"). Landmarks of the visual field (upper/lower field, meridians, and center of gaze) are represented by symbols depicted in the inset. V1 and V2 are shaded by their field signs (dark red, mirror image; dark blue, nonmirror image). (**B**) DM neurons in the model are represented by open circles arranged in a grid (rows are illustrated with horizontal red lines, and columns with vertical blue lines). Receptive field locations are constrained by within-area smoothness (purple arrows) and between-area congruence (green arrows). The latter constraint operates among neighboring DM and V2d neurons (filled circles). (**C**) One particular retinotopy produced by the model, visualized as the cortical grid projected to the visual space. As in (B), rows of neurons are connected by red lines, and columns by blue lines. (**D**) The same retinotopy visualized in the cortical space, where each node of the grid is shaded with a color representing the polar angle of its receptive field (the color scale is illustrated in Fig. 2B). The eccentricities of the receptive fields are visualized with dashed white contours. V1d/v, the dorsal and the ventral part of the primary visual area; V2d/v, the dorsal and the ventral part of the secondary visual area; DM, the dorsomedial visual area; VM, vertical meridian; HM, horizontal meridian; C, caudal; R, rostral; M, medial.

ventral and dorsal cortex, respectively (Fig. 1A). This anatomical configuration allows topographic continuity to be maintained by retinotopic maps that mirror each other relative to the V1/V2 boundary, which corresponds to the representation of the visual field's vertical meridian. The gradient of the polar angle representation is reversed across this boundary, resulting in V1 and V2 having opposing field signs [defined as the clockwise angle between the eccentricity gradient and the polar angle gradient; (*5*)]. Here, we focused on the region of the primate visual cortex immediately rostral to the lower quadrant representation of V2 (dorsal V2 or V2d), a region where the concentric arrangement of V1 and V2 gives way to a patchwork of smaller areas (*9*–*11*, *18*–*20*). This transition introduces a new level of complexity to retinotopy, because in this scenario, V2d could be simultaneously adjacent to the upper and lower field representations of a given rostral area, among other possibilities (Fig. 1A). What would the retinotopy of this area look like under the constraints of topographic continuity?

To address this question, we simulated the formation of a retinotopic map adjacent to the rostral border of V2d, by extending a general framework ("elastic net") for modeling the development of cortical topographic maps (*1*, *21*). In this model, neurons of a small, elongated cortical area were distributed on a 30 × 15 grid representing the surface of the cortex (Fig. 1B). For the purposes of presentation, we will refer to this model area as the dorsomedial area (DM), a name that reflects its location in the primate brain (*18*–*20*). Each neuron was associated with a receptive field; the receptive field centers were initialized using a random process and were updated in an iterative optimization process to cover the visual field up to 10° of eccentricity. Examples of map development in the optimization process are given in fig. S1 and movies S1 and S2. The maximization of the coverage of the visual field was constrained by two forms of topographic continuity: within-area smoothness of representation and between-area congruence. These two constraints were weighted by the β_1 and β_2 parameters, respectively (Fig. 1B). For smoothness, increasing β_1 prioritizes matching receptive field centers of neighboring neurons within the model area DM. For congruence, increasing β_2 prioritizes matching receptive field centers of neighboring neurons on the V2d/DM border. Although the model area is surrounded by other areas rostrally, its retinotopy was assumed to be only influenced by V2d. We expected the influence of V2 to dominate the formation of the DM map, given that occipital areas develop according to a caudal to rostral gradient (*12*–*14*). In addition, the retinotopy of V2 at the V2d/DM boundary was assumed to be fixed (representing the lower visual field adjacent to the horizontal meridian) because the retinotopy of V2d is powerfully constrained by that of V1. This is evidenced by the fact that the retinotopic organization of V2 is invariant across primates of different sizes, ecological niches, and taxonomic groups (*3*, *6*, *22*, *23*).

Systematic representations of the visual field resembling retinotopic maps in the visual cortex were formed over a wide range of β_1 and β_2. We visualize the resulting maps in two complementary formats: as cortical sheets projected to the visual space (Fig. 1C) and as maps of visual field coordinates in the cortex (Fig. 1D). In the first format ["back-transformed maps"; (*24*)], the grid representing the cortical sheet in Fig. 1B is projected onto the visual space, by translating the nodes to the associated receptive field positions (*24*, *25*). The topology of the cortex is represented by line segments connecting neighboring nodes. In this format, it can be seen that under certain settings of β_1 and β_2, a twist in the retinotopy can occur (Fig. 1C, fig. S1, and movie S1).

Maps with inhomogeneous field sign can emerge from the model

We found that the macroscopic organization of the resulting retinotopic map depended on the settings of the model parameters (Fig. 2). At moderate levels of β_1 and β_2, the resulting retinotopy resembled that expected from conventional retinotopic maps: The eccentricity and polar angle maps were continuous, and the entire map had the same field sign (Fig. 2, A and B). As the smoothness constraint (β_1) is decreased, however, the map can become divided into two regions with opposite field signs (Fig. 2, E and F). In these maps, simulating the displacement of an electrode from the lateral end to the medial end of the model area (blue arrow in Fig. 2E) yielded receptive fields that followed an "S"-shaped trajectory (Fig. 2G)—a distinctive pattern not observed in conventional maps

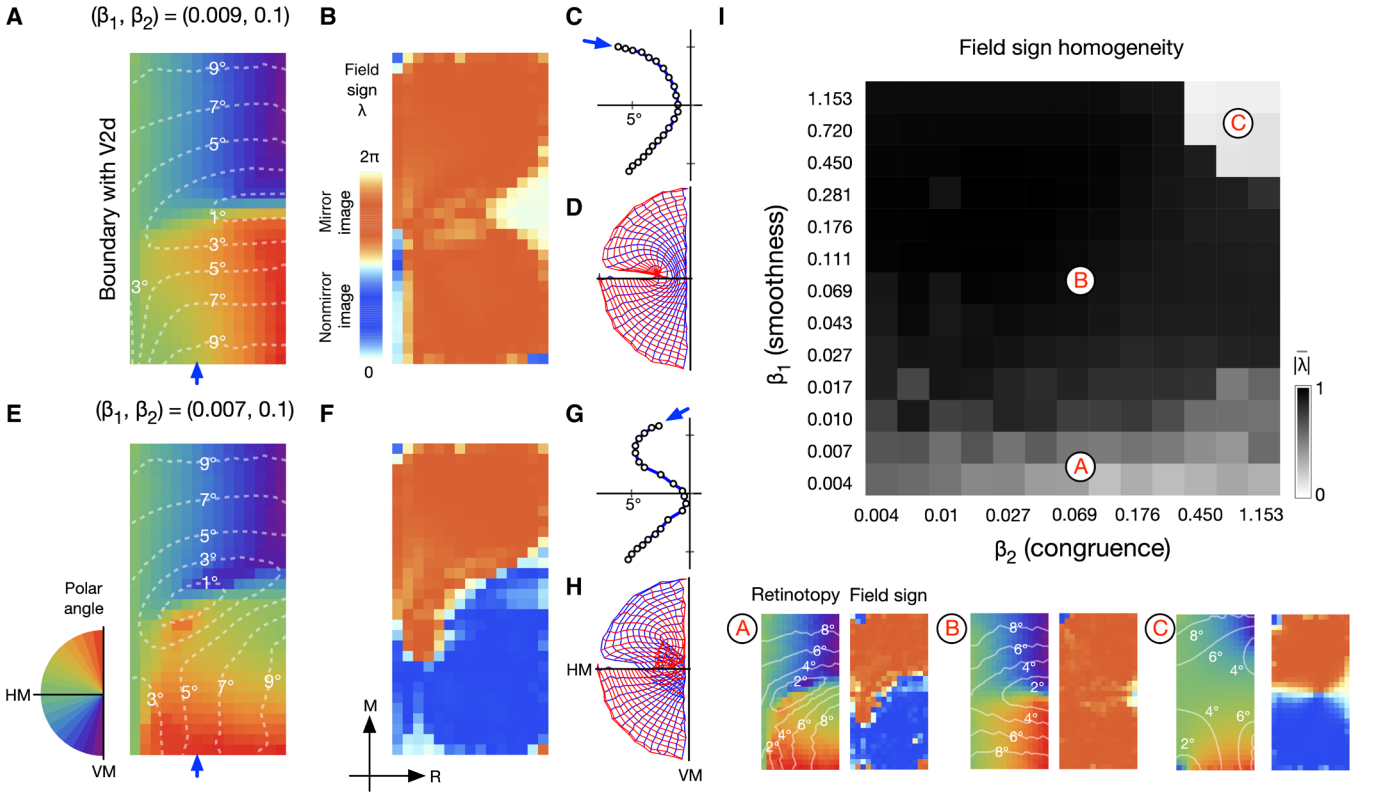

Fig. 2. The dependency between the developed retinotopy and the modeling parameters. (**A**) Conventional retinotopy produced by the model; colors represent polar angle, and dashed white contours represent eccentricity. (**B**) Field sign at each location. (**C**) The progression of receptive field locations, if they are sampled on a path in the direction indicated by the blue arrow in (A). (**D**) The same map as in (A), illustrated in visual space. (**E** to **H**) A "twisted" retinotopy produced by the model. (**I**) The relationship between the two parameters and the field sign of the resulting map. The gray scale indicates field sign homogeneity ($|\bar{\lambda}| = 0$, balanced mirror and nonmirror image field sign; $|\bar{\lambda}| = 1$, mirror image field sign). Regions indicated by "A," "B," and "C" correspond to the three types of maps illustrated in the bottom row.

(Fig. 2C). Comparing the two maps in visual space (Fig. 2, D and H), it can be appreciated that the S-shaped trajectory is due to a twisting of the map, as evident from the fact that the relationship among the blue and the red lines in the back-transformed maps is reversed in the upper visual field, but not in the lower visual field. Given the random initialization, the model can also generate maps where the representations of the two quadrants are flipped relative to the situation shown in Fig. 2 (A and E); in those situations, the field signs are also reversed (see fig. S2B).

The relationship between the resulting retinotopy and the two parameters was explored systematically. To measure the homogeneity of field sign in a map, we calculated $\bar{\lambda}$, the vector average of field sign across the map. As the retinotopy developed was dependent on the initialization of the map (see fig. S2B), $\bar{\lambda}$ was also averaged across 30 random initializations. For balanced mixtures of mirror image and nonmirror image field signs, the length of the vector $\bar{\lambda}$ (denoted by $|\bar{\lambda}|$) is close to 0; but for maps dominated by one field sign, $|\bar{\lambda}|$ is close to 1. The homogeneity index $|\bar{\lambda}|$, plotted in Fig. 2I, shows that different combinations of β_1 and β_2 allowed three types of maps to be formed: the two types described above (type A and B in Fig. 2I) and a third type of map with inhomogeneous field signs, produced at high values of β_1 and β_2 (type C). In this map, the twist is so severe that the representation of the fovea in the lower field is displaced from the rest of the lower field representation. This retinotopy does not seem to correspond to the known organization of any visual area yet described, suggesting that the model explores a parameter space larger than is biologically plausible. When the smoothness parameter β_1 was made lower than the range illustrated in Fig. 2I, the maps developed became increasingly fragmented and became unorganized if β_1 was set to 0 (fig. S2E).

Quantitative mapping revealed an inhomogeneous field sign map in the dorsomedial visual cortex

We have shown that it is possible for twisted maps to develop under a simple model, but is there empirical evidence for such maps in the visual cortex? The extrastriate region rostral to V2d in nonhuman primates offers a promising target to test the predictions of the model. On the basis of histology, connectivity, and single-unit electrophysiology, some studies have proposed that this region contains an area representing both the upper and lower quadrants of the visual field, with a discontinuity in retinotopy separating the two representations (*19*). However, the proposed organization was based on single electrode recording data, where receptive fields were mapped qualitatively and recording sites were distributed unevenly across the cortical surface. The inherent limitations of the methodology led to alternative interpretations, according to which the same region contains areas with more conventional retinotopy (*11*, *17*, *18*).

To clarify the organization of this controversial region, we sought to produce high-resolution, evenly sampled maps, using 10 × 10 multielectrode arrays with 400-μm electrode spacing, in five hemispheres of four marmoset monkeys (*Callithrix jacchus*). For each channel in the array, the receptive field of the sampled neuron was

mapped quantitatively with small flashing squares displayed at randomized locations on the monitor. On the basis of the evoked responses, the coordinates of receptive field centers were extracted. Gradients of eccentricity and polar angle were then calculated to estimate the local field sign of the individual channel. The process is illustrated in a representative case (CJ138) in Fig. 3. Additional cases are illustrated in more detail in fig. S3. Our data indicated that the cortex immediately rostral to V2d contains a representation of the contralateral visual field covering at least 20° in eccentricity (Fig. 4B). The upper field is represented laterally (referred to here as DM+), and the lower field medially (DM−). Both DM+ and DM− border V2d along a continuous representation of the horizontal meridian. This organization is consistent with the proposed retinotopy of area DM (Fig. 4A) (*18*–*20*), but not with the interpretation that postulates the existence of an additional thin strip of "area V3" (representing only the lower visual field) sandwiched between V2d and DM (*17*).

Unusual features of DM retinotopy are consistent with the twisted topography model

Earlier work (*16*, *19*) has suggested that the transition between DM+ and DM− includes a "map discontinuity" (arrow in Fig. 4A)—a sudden jump of receptive field centers between closely spaced recording sites, which violates topographic continuity. Our quantitative mapping data indicated that the retinotopy in this region is indeed unusual: The representations of the central visual field of DM+ and DM− are disjoint (Fig. 5A), and crossing the DM+/DM− boundary resulted in an S-shaped trajectory of receptive field centers across the horizontal meridian (Fig. 5C), similar to the pattern produced by the computational model (Fig. 2G). However, the receptive fields of adjacent recording sites still overlapped substantially, showing no violation of topographic continuity.

The eccentricity gradient along the medial-lateral axis is plotted in Fig. 5B. The maps suggest that a regular sampling of recording sites from lateral to medial increases the eccentricity of the receptive field (positive gradient, displayed in a red color scale), except in a narrow region that has the opposite effect on the eccentricity (negative gradient, displayed in a blue color scale). The map discontinuity suggested by previous studies is therefore more accurately characterized as a thin strip of cortex (~1 mm) with an eccentricity gradient that rapidly reverses polarity (the regions indicated by the orange contours in Fig. 5, A and B).

The local field sign maps in Fig. 5E show that although the retinotopy of DM+ and DM− was individually coherent, they had opposing field signs (DM+, nonmirror image; DM−, mirror image). This is typically taken as evidence that they are two different areas (*9*, *10*); however, it should be noted that field sign is intended to be used to detect the mirroring of retinotopic maps (such as V1 and V2), which is not the case for DM+ and DM−. The modeling result (Fig. 2) suggests that the DM map is better explained by twisting the retinotopic map of a single area, because it predicts the S-shaped trajectory across the horizontal meridian and the arrangement of field signs. To further support this conclusion, we tested whether other physiological characteristics such as receptive field size, cortical magnification factor, and orientation selectivity were similar in DM+ and DM−. The results of this analysis were consistent with the interpretation that these sectors are part of a same visual area (fig. S4).

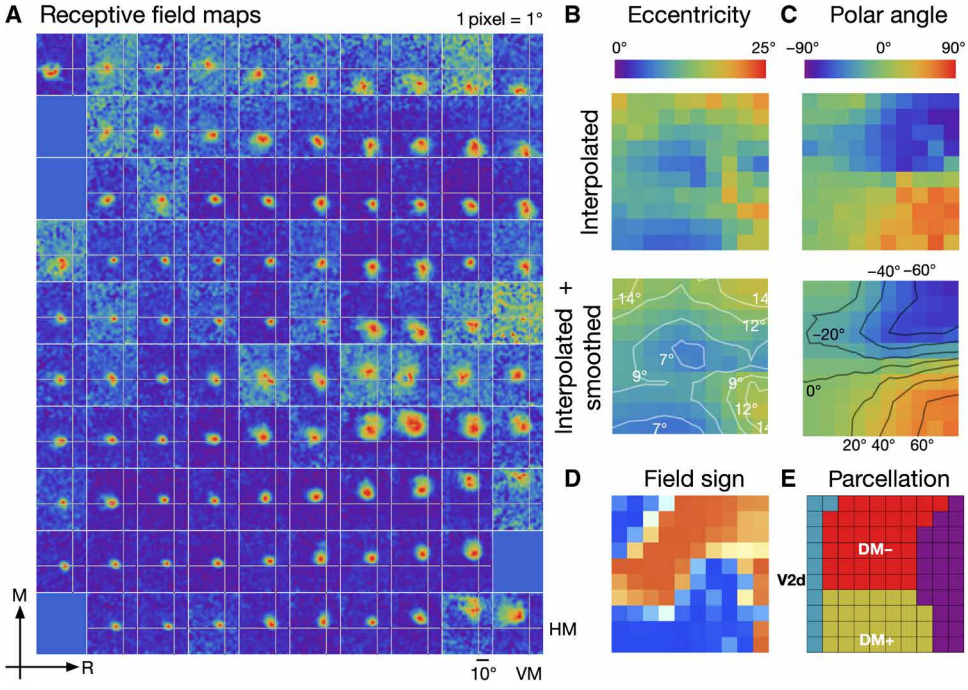

Fig. 3. Quantitative receptive field mapping (case CJ138). (**A**) Receptive fields for all active channels in the 10 × 10 multielectrode array were mapped with a flashing square stimulus displayed on randomized locations. The color scale represents the magnitude of the evoked responses. The cross-hair inside each map represents the estimated HM and VM. (**B**) Coordinates of the receptive fields were extracted. The eccentricity map was generated by interpolation and smoothing. (**C**) So was the polar angle map. (**D**) The gradients of eccentricity and polar angle were estimated for field sign calculation. (**E**) Boundaries of areas were identified. The retinotopic maps are illustrated in the same formats as in Fig. 3.

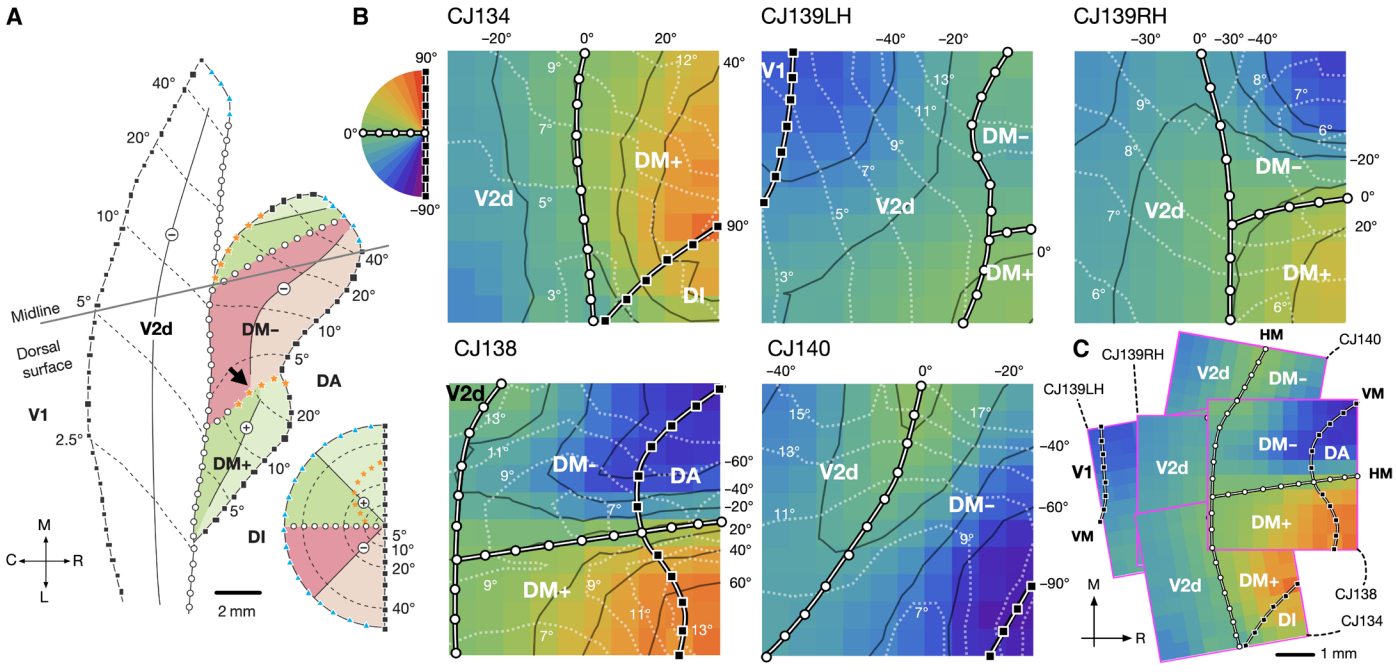

Fig. 4. High-resolution retinotopy of the dorsomedial cortex. (**A**) Schematic summary of one of the models of the organization of dorsomedial cortex in the marmoset (*16*). The inset at the bottom right illustrates the color scheme used to illustrate different segments of the visual hemifield in the proposed area DM. The arrow indicates the location of the putative map discontinuity. (**B**) Retinotopy of five hemispheres from four animals (identifiers of the cases are prefixed by "CJ"), estimated from the quantitative procedure illustrated in Fig. 3. The color scale represents polar angles. Polar angle contours are indicated by solid black contours and numbers in black. Eccentricities are indicated by dashed white lines and numbers in white. Inset: The color scale for representing polar angles in (B) and (C). The HM (polar angle = 0°) is indicated by thick lines overlaid with circles. The VM (polar angle ±90°) is indicated by thick lines and squares. (**C**) Composite summary of the spatial relationships shown in (B) based on array implantation sites identified on histological sections (fig. S6). V1, primary visual area; V2d, dorsal portion of secondary visual area; DM+/DM−, upper/lower field representation of the dorsomedial (DM) area; DA, dorsoanterior area; DI, dorsointermediate area.

The formation of twisted maps depends on the topological relationship between upper and lower quadrant representations

Our computational model (Fig. 2) suggests that the unusual retinotopy of the dorsomedial cortex (Figs. 4 and 5) can be explained by the twisting of an otherwise conventional map. We conducted additional simulations of map formation in the early visual cortex under different topological configurations to further explore the hypothesis that the emergence of this type of twisted map is associated with a situation where both the upper and the lower quadrants are represented in a spatially defined region that is adjacent to a representation of a single (lower) quadrant—as in the cortex rostral to V2d (*9*–*11*).

Whereas it has been proposed that the V2 map emerges naturally from its configuration relative to V1 (*3*), this has not been the subject of formal modeling studies. Thus, we first modeled the formation of a strip-like map under the constraint that its caudal border adjoined a large portion of the vertical meridian representation of V1 (the region shaded in blue in Fig. 6A). The results show that a V2-like nonmirror image map (Fig. 6B) emerges across a wide range of combinations of parameters. As in the primate cortex, the representations of the lower and the upper visual quadrants were split into a dorsal and a ventral branch; the horizontal meridian was represented at the rostral border, and the iso-eccentricity lines were perpendicular to the iso-polar-angle lines.

Having confirmed that the model predicted a V2-like map, we next simulated the formation of third tier areas with different topological relationships to the rostral border of V2. It has been proposed that in most mammals, the cortex adjacent to the foveal representation of V2 is part of an elongated map, usually referred to as area 19 or V3 (*11*, *17*, *20*, *26*, *27*). Thus, we next modeled map formation in an elongated sector of the third tier cortex that reflected this topology and constrained by the retinotopy of V2 along its caudal border (the region shaded in purple in Fig. 6A). What emerged was a mirror image map, in many ways similar to the traditional view of the organization of area V3, or the ventrolateral posterior (VLP) area proposed by electrophysiological mapping studies in the marmoset (*11*, *26*).

The above result shows that a relatively simple, homogeneous field sign area results from our model, in the scenario where this area is adjacent to representations of both quadrants of another retinotopically well-organized area. Previous studies have suggested that the degree of elongation of an area can also influence the type of retinotopic map formed by a self-organizing algorithm (*25*). Thus, to test this further, we studied the scenario in which an area with dimensions similar to those of the model DM (Fig. 1) was displaced laterally, such that its caudal border was centered on neighboring foveal representation of V2 (the region shaded in pink in Fig. 6A). In this scenario, the congruence constraint included both the upper and the lower visual quadrants. The map that emerged (Fig. 6D) was also a nonmirror image representation. When the weights of smoothness and congruence were manipulated, no combination of β_1 and β_2 in the above three simulations gave rise to the type of twisted map illustrated in Fig. 2 (see fig. S5 for detail). This outcome is consistent with the hypothesis that topographic twists in retinotopic

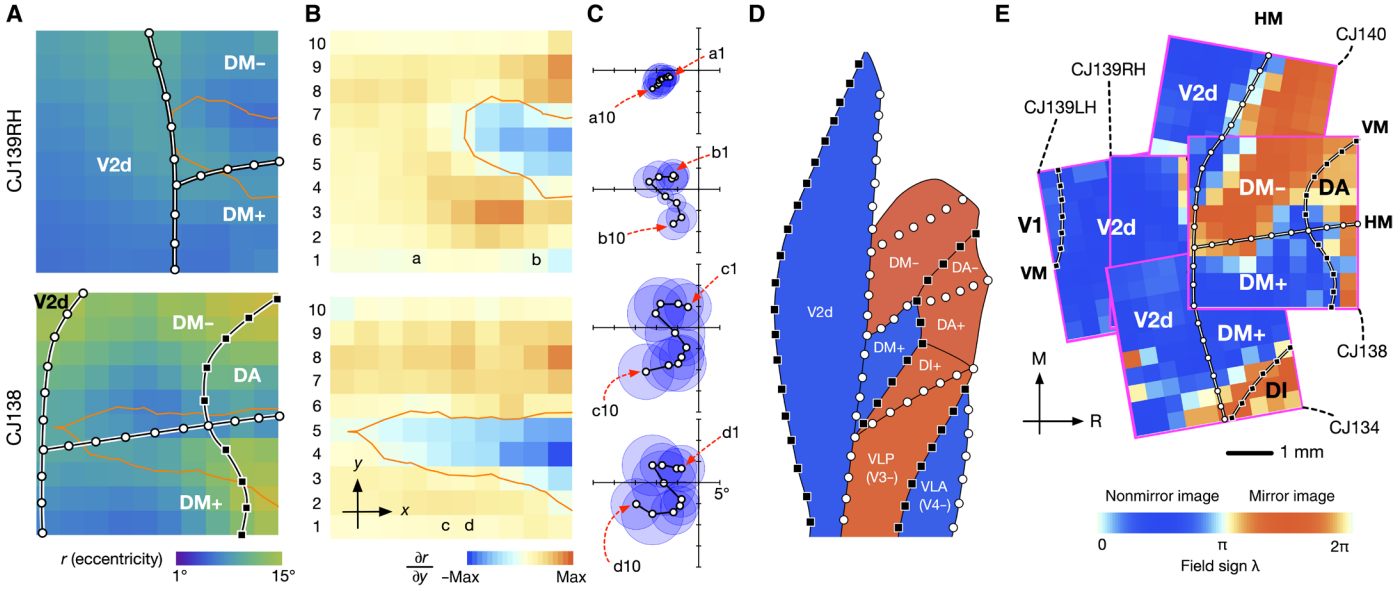

Fig. 5. Unusual features of DM retinotopy and field sign summaries. (**A**) Eccentricity maps of two selected cases. (**B**) Maps of partial gradient of eccentricity with respect to the medial-lateral axis (*y* axis) of the electrode arrays. The regions shaded in a blue color scale (enclosed by the orange contours) correspond to sites where the eccentricity of the receptive field rapidly decreased in the lateral-to-medial direction. The contours are duplicated in (A). (**C**) Representative sequences of receptive fields associated with channels in columns of the electrode arrays. The association between the receptive fields and the channels is identified by letters (columns) and numbers (rows). In these plots, receptive field locations were not smoothed across channels. (**D**) Summary of the field signs for areas in the dorsomedial region of the marmoset visual cortex. The field signs for areas DM, DI, VLP (or V3), and VLA (or V4) were inferred from published maps (*26*). (**E**) Field sign maps estimated for the five cases. The locations of the arrays were established by histological examination of flat-mounted sections and visualization of the arrays relative to the borders of V1 and V2 (see fig. S6). VLP, ventrolateral posterior area; VLA, ventrolateral anterior area.

maps are associated with specific topological relationships between adjacent maps, such as the one found in the primate dorsomedial cortex rostral to V2.

DISCUSSION

Using a simple computational model, we demonstrated that for concentrically organized areas such as V1 and V2, the mirror/nonmirror image pattern of representation follows naturally from topographic continuity (Fig. 6, B and C). However, for the third tier visual cortex, where the concentric organization makes a transition to a patchwork of smaller areas, this model predicts different outcomes, depending on the location of the area relative to V2 and the relative strength of within-area and across-area continuity constraints. In particular, the model shows that a single area with regions of mirror and nonmirror image representation is possible (Fig. 2F). The latter prediction was confirmed empirically by quantitative electrophysiological mapping of area DM in marmoset monkeys. In addition, several unusual characteristics observed in the mapping data were consistent with the model's predictions: disjointed representations of the central visual field in DM+/DM− (Fig. 5A), the S-shaped trajectory of receptive field centers across the DM+/DM− boundary (Fig. 5C), and the field sign of DM+ being the same as that of neighboring V2d.

The modeling results help clarify the organization of the dorsomedial cortex, which has been controversial for decades. Because of the similarity between DM+ and DM− in terms of histology, connectivity, receptive field size, cortical magnification factor, and response properties, the modeling result further supports the notion that these are parts of the same area, which is located immediately rostral to V2d. This organization is unlikely to be unique to the marmoset, as recent studies in owl monkeys (*9*) and macaques (*10*) reported compatible results in the cortex rostral to V2, but subdivided the cortex differently by virtue of prioritizing the homogeneity of field sign within areas. However, both of these proposals resulted in areas with unbalanced representations of the upper and lower quadrants, which have been regarded as unparsimonious (*15*).

Continuity, and its violation, is fundamental to theories of topographic map formation (*1*, *2*). Two types of discontinuity in topographic maps can be distinguished (*16*, *28*): field discontinuities (i.e., adjacent regions on the visual field mapped to nonadjacent regions on the cortical surface) and map discontinuities (i.e., nonadjacent regions on the visual field mapped to adjacent regions on the cortical surface). While field discontinuities are well documented and appear ubiquitous in the primate cortex (*3*, *7*, *16*), the existence of map discontinuities has been controversial. We showed that the transition zone at the DM+/DM− boundary is more appropriately characterized as a thin strip of cortex with rapidly changing gradient rather than a true discontinuity (Fig. 5B). A map discontinuity has also been reported to exist at the border between hand and face representations in the somatosensory cortex (*29*), but the fine topography of this region is yet to be studied with fully quantitative techniques.

We showed that different types of retinotopic maps can emerge depending on the balance between two forms of topographic continuity: within-area smoothness in representation and between-area congruence. Smoothness and congruence constraints do not map one to one onto explicit physiological or anatomical properties of visual circuits. Rather, they likely represent the combined effects of multiple factors, such as receptive field overlap, the density of the columnar structure of an area, the extent of intrinsic connections,

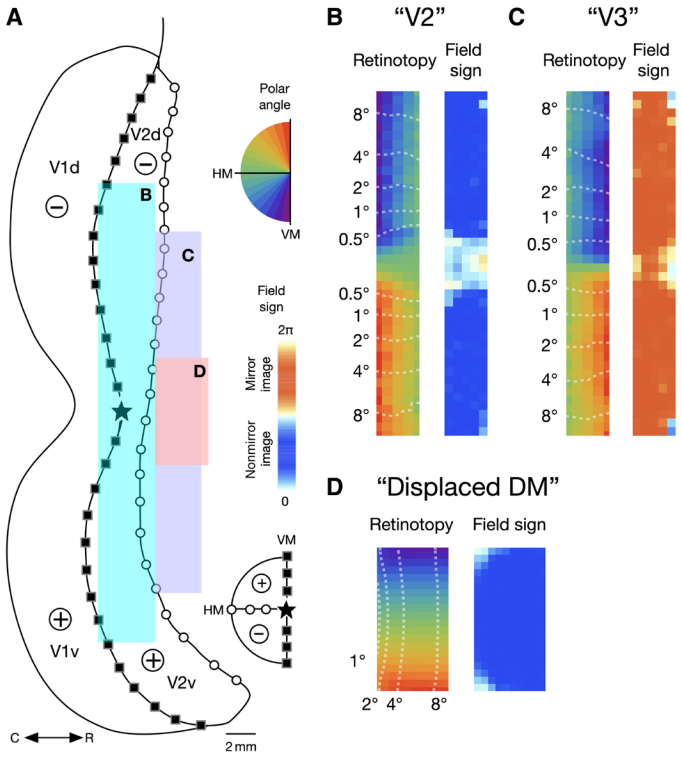

Fig. 6. Modeling different scenarios of map formation in the early visual cortex. (**A**) Schematic illustration showing the spatial relationships among the three modeling scenarios whose results are shown in (**B**) (indicated by the cyan rectangle), (**C**) (indicated by the purple rectangle), and (**D**) (indicated by the pink rectangle). (B) Retinotopy map (left) and the field sign map (right) developed in a configuration similar to area V2. The maps are displayed in the same format as in Fig. 2. The β_1 and β_2 parameters were set to (0.04, 0.04). (**C**) Retinotopy developed in a configuration similar to the traditional view of V3. (β_1, β_2) = (0.123 0.123). (**D**) Retinotopy developed if an area with a dimension similar to DM was displaced to be adjacent to the foveal representation of V2. (β_1, β_2) = (0.05 0.05). Additional details about the simulation are provided in fig. S5.

and the wiring cost of the underlying circuits. Our simulation indicates that the DM map was formed in a regime where between-area congruence was prioritized over within-area continuity. This situation may emerge when topographic maps in different areas develop asynchronously, with a preexisting or more developmentally advanced map in an early-maturing area constraining the possible receptive field locations at the border with a late-maturing area (*12*–*14*).

During development, the constraints are likely mediated by horizontal intrinsic connections within the cortex. It has been shown experimentally that horizontal intrinsic connections are more extensive in early postnatal life than in adulthood (*30*) and that they span the border between areas rather than stopping abruptly at borders (*31*). Although corticocortical connections exist prenatally, there is ample opportunity for postnatal refinement by mechanisms such as the pruning of connections and activity-dependent sprouting of new intrinsic pathways (*32*, *33*). Furthermore, the fact that different areas in the cortex anterior to V2 have different cellular and neurochemical structures, both during development and in adulthood (*11*, *13*, *34*), indicates that their limits are, at least to some extent, determined by molecular specification steps (*35*, *36*). Thus, our model assumes that the formation and refinement of the maps occur within relatively stable boundaries.

Our model further indicates that the topological relationship between adjacent maps is important in determining the occurrence of a twisted map. Among the scenarios tested, this type of map occurred only when representations of both quadrants are formed in a defined region adjacent to a representation of a single quadrant. However, the model also indicates that different, topographically stable solutions to the problem of maximizing topographic continuity may be possible, depending on factors such as the relative extent of different areas and the relative strength of the two constraints. It is possible that this may lead to different configurations of a homologous area in different species [for discussion, see (*11*)], as well as a degree of individual variability within a species (*37*). According to the model, whether the upper quadrant representation occurs in the lateral or the medial segment of DM depends on initialization (fig. S2B). In contrast, the existing data (*5*, *11*, *19*, *20*) consistently show that the lateral segment of area DM represents the upper quadrant (area DM+ in Fig. 4A). This suggests that the formation of maps can be biased by other factors, such as asynchronous maturation gradients within an area (*12*, *38*).

Our simulation and experimental results indicate that the arrangement of field sign in the extrastriate cortex can be complex: A single area can have segments of opposing field signs, and boundaries between areas are not necessarily identifiable by field sign (Fig. 5D). The interpretation of field sign for area parcellation therefore demands a nuanced approach, which takes into account the context of the global map across areas, cyto- and myeloarchitecture, and connectivity. The present results indicate that some of the uncertainties and controversies in the mapping of extrastriate areas might be due to complex local topographies occurring at the microscopic level, which might not be detectable by the typical resolution of functional magnetic resonance imaging and optical imaging. Wide-field two-photon imaging, which has been successful for mapping the rodent visual cortex (*8*), presents a promising approach for elucidating these controversies in the primate extrastriate cortex.

It is also important to acknowledge that further extension of the current model will be needed to capture finer details of the observed retinotopy. For example, although both the model and the in vivo data revealed S-shaped trajectories of receptive fields near the DM+/DM− transition zone, which are a signature of the twisted map, details differ: The model trajectories show receptive fields crossing the horizontal meridian close to the center of the fovea, whereas the empirically observed receptive fields are centered parafoveally (*18*, *19*). It remains unclear whether this is due to the limited sampling density afforded by our electrode arrays or if it is related to the observation that, in DM, the center of the fovea is only covered by the boundaries of its relatively large receptive fields (*19*). Incorporating parameters that reflect receptive field extents in the different areas and realistic shapes of visual areas is likely to advance our understanding of this issue. Furthermore, this work was informed by findings about the development of cortical maps, but additional insights on the development of extrastriate areas, as well as its relationship to the computational theory of map formation, deserve further investigation. The model presented was designed specifically to provide insights about a region of the visual cortex where the concentric organization of V1 and V2 makes a transition to a patchwork configuration. It does not address broader-scope questions such as the organizational and developmental differences between the dorsal and the ventral visual cortices (*13*, *14*), the large-scale development of area complexes, such as the clusters proposed for the human visual

cortex (*7*, *39*), the interaction between temporal maturation gradients centered in different areas (*4*, *12*, *14*), or possible additional constraints imposed by long-range connections with nonadjacent areas. Systematic exploration of self-organizing models (*21*, *25*) informed by physiological results and further mechanistic insights about the specification of area boundaries in development will be needed to further advance this field.

MATERIALS AND METHODS

Simulation

An extension of the elastic net algorithm (*21*) was used to solve the proximate minimal path length problem (*1*). The model consisted of neurons with point receptive fields (y_j) initialized to randomized locations on the contralateral visual hemifield within 10° of eccentricity (see below). These receptive fields are arranged topologically in a 30 × 15 grid, and they were updated iteratively using gradient descent to minimize the energy function

$$-k\sum_i \log\sum_j \Phi(x_i, y_j, k) + \beta_1 \sum_j \sum_{j' \in N(j)} \|y_{j'} - y_j\|^2 + \beta_2 \sum_{j \in B} \sum_{j' \in N_{V2}(j)} \|z_{j'} - y_j\|^2 \quad (1)$$

The first term is a "coverage term" that forces y_j to converge to 500 fixed points (x_i) distributed regularly on the visual hemifield up to 10° of eccentricity, with a density that dropped off with eccentricity (density ∝ eccentricity$^{-0.4}$; see the red dots in the inset of fig. S1A). $\Phi(x_i, y_j, k) = \exp\left(\frac{-\|x_i - y_j\|^2}{2k^2}\right)$, where k is an annealing factor that was initialized to 30.0 and reduced by 0.5% for each iteration. The regular distribution of x_i was implemented with the Vogel method. The coverage term is followed by two regularization terms to enforce topographic continuity, which were weighted by two parameters β_1 and β_2. The first regularization term enforces the smoothness of the retinotopy, where $N(j)$ denotes sites on the 30 × 15 grid that neighbor site j. The second regularization term enforces congruence with the retinotopy of V2d at the caudal boundary of DM (denoted by $\boldsymbol{B}$), where $N_{V2}(j)$ denotes sites in V2d that neighbor site j in DM. V2 receptive fields are centered at $z_{j'}$, which are fixed points on the horizontal meridian, following the magnification factor of V2. The range of eccentricity at the DM/V2 boundary was 2° to 10.0°. The dimension of the grid (corresponding to ~5.5 mm by 2.75 mm on the cortex) and its relationship with V2 retinotopy were chosen to roughly correspond to the relationship between areas DM and V2 (Fig. 4A). The map was initialized using the following randomized process: Each y_j was assigned to a random choice (with replacement) of the 500 fixed points x_i, and it was then disturbed by a two-dimensional noise following the standard normal distribution (which can displace the coordinates up to 3° in eccentricity).

For the simulations of the V2 and V3 maps (Fig. 6, B and C), grids of 40 × 5 neurons were used in the elastic net to approximate the elongated shapes of the simulated areas. The simulated V2 corresponded to 30 mm by 3.75 mm in cortical space, and the simulated V3 corresponded to 22 mm by 2.75 mm. The retinotopic coordinates of neurons in V1 and V2 that constrained the models were calculated on the basis of published cortical magnification functions for the marmoset (*40*, *41*). The lengths of the two areas were chosen such that the congruence constrains were limited to ~10° of eccentricity.

For the "displaced DM" simulation (Fig. 6D), a grid of 20 × 10 neurons was used, corresponding to 7 mm by 3.5 mm cortical space. The dimension was chosen to be slightly larger than the dimension (5.5 mm by 2.75 mm) used in the DM simulation, so that the congruence constraint from the rostral border of V2 corresponded to the horizontal meridian up to ~1° in eccentricity. Because of the high cortical magnification factor of V2 near the foveal representation, the 5.5-mm length would correspond to a very small segment of the horizontal meridian, which appeared to be implausible.

For all three simulations, elastic nets were optimized to represent the visual field up to 10° in eccentricity, which was sampled by 400 fixed points. For the simulation of V3 and the displaced DM, the congruence constraint from V2, rather than the exact horizontal meridian, was set to be 10° (in polar angle) away from the horizontal meridian, so that the upper and lower quadrant representations of V2 near the rostral border could be distinguished.

Field sign

Field sign (λ) is defined as the clockwise angle between the eccentricity gradient and the polar angle gradient (*5*). The same procedure was used to calculate the field signs of maps produced by simulations and by electrophysiological recordings (see below). For calculating the gradients, the receptive field coordinates were smoothed by moving window averaging. The field signs calculated for each neuron were then smoothed by moving window averaging across the grid. For visualization, the calculated field sign was compressed by a sigmoid function (*5*) and then displayed with a color scale such that nonmirror image maps ($0 < \lambda < \pi$) appear bluish and mirror image maps ($\pi < \lambda < 2\pi$) appear reddish.

Field sign homogeneity index $|\overline{\lambda}|$

To quantify the homogeneity of field signs in a retinotopic map, the local field signs were converted to unit vectors, which were then averaged across the map (and across multiple maps if the simulation was repeated). The result was a vector $\overline{\lambda}$. The length of the vector $|\overline{\lambda}|$ measured the homogeneity of the field signs, because opposing field signs in an inhomogeneous map canceled each other, producing a small length, closer to 0. A map with similar local field signs, on the other hand, would produce a length closer to 1. The representations of the two quadrants can be flipped in the model DM, which reverses the field sign (see fig. S2B). For the analysis of $|\overline{\lambda}|$ illustrated in Fig. 2I, the maps were normalized such that the lateral segment always represents the upper quadrant.

Experimental preparation

Experiments were conducted in accordance with the Australian Code of Practice for the Care and Use of Animals for Scientific Purposes. All procedures were approved by the Monash University Animal Ethics Experimentation Committee. In four marmoset monkeys (*C. jacchus*), surgical anesthesia was induced by intramuscular injection of alfaxalone (Alfaxan; 8 mg/kg). Under anesthesia, the animal was injected with an antibiotic (Norocillin; 25 mg/kg) and dexamethasone (Dexason; 0.3 mg/kg). A tracheotomy was performed, and the femoral artery was cannulated. The animal was positioned in a stereotaxic frame, and a craniotomy and durotomy were performed over the dorsomedial extrastriate cortex. For the duration of the recording session, the animal was maintained on infusion of sufentanil citrate (Sufenta Forte; 250 μg/5 ml), pancuronium bromide (Pancronium; 4 mg/2 ml), dexamethasone (Dexapent; 5 mg/ml), xylazine (Xylazil-20; 20 mg/ml), and salts and nutrients (0.18% NaCl/4% glucose solution, Synthamine-13, and Hartmann's solution) and

ventilated with a nitrous oxide and oxygen mixture (7:3). The animal's body temperature was kept at a steady 38°, measured by rectal thermometer. The eye contralateral to the craniotomy was held open, and atropine (Atropt; 1%), phenylephrine, and carmellose sodium (Celluvisc) eye drops were applied before a contact lens was inserted to focus the eye at a viewing distance of 20 to 40 cm. The ipsilateral eye was protected with carmellose sodium, closed, and occluded.

Electrophysiology

"Utah" arrays (10 × 10; Blackrock Microsystems, Salt Lake City, United States) with 96 active channels were implanted in the expected location of the border between V2 and the areas rostral to it, using a pneumatic insertion tool. The position of the array was planned using stereotaxic coordinates (*42*) in vivo and verified with flat-mount histology postmortem (fig. S6). Electrodes were 1.5 mm long and spaced at 400-μm intervals. The raw voltage signal was recorded at 30 kHz using a Cerebus system (Blackrock Microsystems, Salt Lake City, United States) and high-pass filtered at 750 Hz. Spikes were detected using automatic thresholding of the local signal. After recording, manual spike sorting was performed offline using a Plexon Offline Sorter (Plexon Inc., Dallas, United States).

Visual stimulation

Following preliminary qualitative mapping of the positions of several receptive fields on a tangent screen, a VIEWPixx 3D (VPixx Technologies, Saint-Bruno, Canada) was positioned at a viewing distance of 350 to 450 mm. This was done in such a way that the receptive fields obtained during the preliminary exploration were located around the center of the monitor. The stimuli were presented at a 120-Hz refresh rate using The Psychophysics Toolbox in MATLAB (*43*). Receptive fields were mapped at 1° resolution with both "on" (white) and "off" (black) squares flashed on a gray background. Squares appeared for 100 ms with a 50- to 100-ms (different in different cases) interstimulus interval.

Retinotopy

To quantify the geometry of the receptive fields, the spike counts elicited by each location of the flashing square stimulus were smoothed with a 5 × 5 Gaussian kernel. A Gaussian function was fitted to the smoothed map (Eq. 2), where (μ_x, μ_y) is the center of the receptive field. The boundary of the receptive field (and therefore its size) was determined by the contour at 15% of the peak response

$$r = c + e^{\frac{1}{2}\left(-\frac{(x-\mu_x)^2}{\sigma} - \frac{(y-\mu_y)^2}{\sigma}\right)} \quad (2)$$

The center of gaze was inferred from the retinotopy, given that at the boundary of visual areas, the progression of the receptive fields reverses its direction at the horizontal or the vertical meridian. For CJ134, CJ138, and CJ140, the locations of the blind spot could be identified in the receptive field maps (fig. S3). Because the representation of the blind spot on the visual field is approximately 15° away from the fovea on the horizontal meridian (*44*), this imposed a strong constraint on the location of the center of gaze.

Cortical magnification factor

The reciprocal of the (linear) cortical magnification factor (*45*) $1/M$ was calculated as $\sqrt{1/M_a}$, where $1/M_a = \mid \det(J) \mid$, with J being the Jacobian matrix of the mapping from the cortex surface to the visual field (*46*). This measures the linear cortical magnification factor M from the areal cortical magnification factor M_a, assuming that the mapping is isotropic. The calculation of J was based on the locations of the measured receptive field centers without smoothing. The estimated $1/M$ was then spatially smoothed.

Orientation tuning

We used drifting sinusoidal gratings to determine the preferred orientation for the units on the array (fig. S4C). Spatial and temporal frequencies were selected to best drive the largest number of units possible and ranged from 0.3 to 1 cycle/° and 2.5 to 4 Hz. Responses were measured for 24 directions, tiling 360° at 15° intervals to motion lasting 400 to 1000 ms. The preferred orientation was determined on the basis of the resultant vector and the bandwidth with the circular variance of the responses (*47*).

Histology

After the completion of data collection, the animal was given a lethal overdose of sodium pentobarbitone (100 mg/kg). The array was removed, and the animal was transferred to a fume hood where it was perfused with buffered saline. The unfixed brain was immediately extracted, and the two hemispheres were separated and physically flat mounted. Flat mounting (fig. S6) was performed by gently dissecting away the white matter of the cortex with dry cotton swabs, with the cortex supported on a piece of moist filter paper (pial surface down). Relaxation cuts were made in the fundus of the calcarine sulcus and at the anterior end of the sylvian sulcus to allow the cortex to lie flat. The cortex was held in fixative between two large glass slides under a small weight overnight and then was soaked in sucrose solution in increasing concentrations (10, 20, and 30%). The flat-mounted hemisphere was then cut in a cryostat to a thickness of 40 μm. Alternate sections were stained for myelin and cytochrome oxidase, which were used to visualize landmarks such as V1 and V2.

SUPPLEMENTARY MATERIALS

Supplementary material for this article is available at http://advances.sciencemag.org/cgi/content/full/6/44/eaaz8673/DC1

View/request a protocol for this paper from *Bio-protocol*.

REFERENCES AND NOTES

1. R. Durbin, G. Mitchison, A dimension reduction framework for understanding cortical maps. *Nature* **343**, 644–647 (1990).
2. N. V. Swindale, The development of topography in the visual cortex: A review of models. *Network* **7**, 161–247 (1996).
3. J. M. Allman, J. H. Kaas, The organization of the second visual area (V II) in the owl monkey: A second order transformation of the visual hemifield. *Brain Res.* **76**, 247–265 (1974).
4. M. G. P. Rosa, R. Tweedale, Brain maps, great and small: Lessons from comparative studies of primate visual cortical organization. *Philos. Trans. R. Soc. Lond. B Biol. Sci.* **360**, 665–691 (2005).
5. M. I. Sereno, C. T. McDonald, J. M. Allman, Analysis of retinotopic maps in extrastriate cortex. *Cereb. Cortex* **4**, 601–620 (1994).
6. M. I. Sereno, A. M. Dale, J. B. Reppas, K. K. Kwong, J. W. Belliveau, T. J. Brady, B. R. Rosen, R. B. Tootell, Borders of multiple visual areas in humans revealed by functional magnetic resonance imaging. *Science* **268**, 889–893 (1995).
7. B. A. Wandell, S. O. Dumoulin, A. A. Brewer, Visual field maps in human cortex. *Neuron* **56**, 366–383 (2007).
8. M. E. Garrett, I. Nauhaus, J. H. Marshel, E. M. Callaway, Topography and areal organization of mouse visual cortex. *J. Neurosci.* **34**, 12587–12600 (2014).
9. M. I. Sereno, C. T. McDonald, J. M. Allman, Retinotopic organization of extrastriate cortex in the owl monkey—Dorsal and lateral areas. *Vis. Neurosci.* **32**, e021 (2015).
10. Q. Zhu, W. Vanduffel, Submillimeter fMRI reveals a layout of dorsal visual cortex in macaques, remarkably similar to New World monkeys. *Proc. Natl. Acad. Sci. U.S.A.* **116**, 2306–2311 (2019).

11. A. Angelucci, M. G. P. Rosa, Resolving the organization of the third tier visual cortex in primates: A hypothesis-based approach. *Vis. Neurosci.* **32**, e010 (2015).
12. J. A. Bourne, M. G. P. Rosa, Hierarchical development of the primate visual cortex, as revealed by neurofilament immunoreactivity: Early maturation of the middle temporal area (MT). *Cereb. Cortex* **16**, 405–414 (2006).
13. I.-C. Mundinano, W. C. Kwan, J. A. Bourne, Mapping the mosaic sequence of primate visual cortex development. *Front. Neuroanat.* **9**, e132 (2015).
14. S. J. Sawiak, Y. Shiba, L. Oikonomidis, C. P. Windle, A. M. Santangelo, H. Grydeland, G. Cockcroft, E. T. Bullmore, A. C. Roberts, Trajectories and milestones of cortical and subcortical development of the marmoset brain from infancy to adulthood. *Cereb. Cortex* **28**, 4440–4453 (2018).
15. S. M. Zeki, Improbable areas in the visual brain. *Trends Neurosci.* **26**, 23–26 (2003).
16. M. G. P. Rosa, R. Tweedale, Maps of the visual field in the cerebral cortex of primates: Functional organisation and significance, in *The Primate Visual System*, J. H. Kaas, C. E. Collins, Eds. (CRC Press, Boca Raton, 2004), pp. 261–288.
17. D. C. Lyon, J. D. Connolly, The case for primate V3. *Proc. R. Soc. Lond. B Biol. Sci.* **279**, 625–633 (2012).
18. J. M. Allman, J. H. Kaas, The dorsomedial cortical visual area: A third tier area in the occipital lobe of the owl monkey (*Aotus trivirgatus*). *Brain Res.* **100**, 473–487 (1975).
19. M. G. P. Rosa, L. M. Schmid, Visual areas in the dorsal and medial extrastriate cortices of the marmoset. *J. Comp. Neurol.* **359**, 272–299 (1995).
20. J. Jeffs, F. Federer, J. M. Ichida, A. Angelucci, High-resolution mapping of anatomical connections in marmoset extrastriate cortex reveals a complete representation of the visual field bordering dorsal V2. *Cereb. Cortex* **23**, 1126–1147 (2013).
21. G. J. Goodhill, D. J. Willshaw, Application of the elastic net algorithm to the formation of ocular dominance stripes. *Network* **1**, 41–59 (1990).
22. R. Gattass, C. G. Gross, J. H. Sandell, Visual topography of V2 in the macaque. *J. Comp. Neurol.* **201**, 519–539 (1981).
23. M. G. P. Rosa, A. P. B. Sousa, R. Gattass, Representation of the visual field in the second visual area in the *Cebus* monkey. *J. Comp. Neurol.* **275**, 326–345 (1988).
24. J. H. R. Maunsell, D. C. van Essen, Topographic organization of the middle temporal visual area in the macaque monkey: Representational biases and the relationship to callosal connections and myeloarchitectonic boundaries. *J. Comp. Neurol.* **266**, 535–555 (1987).
25. F. Wolf, H.-U. Bauer, T. Geisel, Formation of field discontinuities and islands in visual cortical maps. *Biol. Cybern.* **70**, 525–531 (1994).
26. M. G. P. Rosa, R. Tweedale, Visual areas in lateral and ventral extrastriate cortices of the marmoset monkey. *J. Comp. Neurol.* **422**, 621–651 (2000).
27. M. G. P. Rosa, P. R. Manger, Clarifying homologies in the mammalian cerebral cortex: The case of the third visual area (V3). *Clin. Exp. Pharmacol. Physiol.* **32**, 327–339 (2005).
28. D. C. Van Essen, J. H. R. Maunsell, J. L. Bixby, The middle temporal visual area in the macaque: Myeloarchitecture, connections, functional properties and topographic organization. *J. Comp. Neurol.* **199**, 293–326 (1981).
29. P. R. Manger, T. M. Woods, A. Muñoz, E. G. Jones, Hand/face border as a limiting boundary in the body representation in monkey somatosensory cortex. *J. Neurosci.* **17**, 6338–6351 (1997).
30. H. J. Luhmann, L. Martínez Millán, W. Singer, Development of horizontal intrinsic connections in cat striate cortex. *Exp. Brain Res.* **63**, 443–448 (1986).
31. R. Malach, T. D. Schirman, M. Harel, R. B. Tootell, D. Malonek, Organization of intrinsic connections in owl monkey area MT. *Cereb. Cortex* **7**, 386–393 (1997).
32. H. Kennedy, R. Douglas, K. Knoblauch, C. Dehay, Self-organization and pattern formation in primate cortical networks. *Novartis Found. Symp.* **288**, 178–194 (2007).
33. C. Darian-Smith, C. D. Gilbert, Axonal sprouting accompanies functional reorganization in adult cat striate cortex. *Nature* **368**, 737–740 (1994).
34. N. Atapour, P. Majka, I. H. Wolkowicz, D. Malamanova, K. H. Worthy, M. G. P. Rosa, Neuronal distribution across the cerebral cortex of the marmoset monkey (*Callithrix jacchus*). *Cereb. Cortex* **29**, 3836–3863 (2019).
35. M. J. Donoghue, P. Rakic, Molecular evidence for the early specification of presumptive functional domains in the embryonic primate cerebral cortex. *J. Neurosci.* **19**, 5967–5979 (1999).
36. J. Homman-Ludiye, J. A. Bourne, Mapping arealisation of the visual cortex of non-primate species: Lessons for development and evolution. *Front. Neural Circuits* **8**, 79 (2014).
37. R. J. Tusa, A. C. Rosenquist, L. A. Palmer, Retinotopic organization of areas 18 and 19 in the cat. *J. Comp. Neurol.* **185**, 657–678 (1979).
38. J. A. Bourne, C. E. Warner, M. G. P. Rosa, Topographic and laminar maturation of striate cortex in early postnatal marmoset monkeys, as revealed by neurofilament immunohistochemistry. *Cereb. Cortex* **15**, 740–748 (2005).
39. M. J. Arcaro, S. Kastner, Topographic organization of areas V3 and V4 and its relation to supra-areal organization of the primate visual system. *Vis. Neurosci.* **32**, e014 (2015).
40. T. A. Chaplin, H.-H. Yu, M. G. P. Rosa, Representation of the visual field in the primary visual area of the marmoset monkey: Magnification factors, point-image size, and proportionality to retinal ganglion cell density. *J. Comp. Neurol.* **521**, 1001–1019 (2013).
41. M. G. P. Rosa, K. A. Fritsches, G. N. Elston, The second visual area in the marmoset monkey: Visuotopic organization, magnification factors, architectonical boundaries, and modularity. *J. Comp. Neurol.* **387**, 547–567 (1997).
42. G. Paxinos, C. Watson, M. Petrides, M. G. P. Rosa, H. Tokuno, *The Marmoset Brain in Stereotaxic Coordinates* (Elsevier Academic Press, Cambridge, MA, 2012).
43. D. H. Brainard, The psychophysics toolbox. *Spat. Vis.* **10**, 433–436 (1997).
44. D. Troilo, H. C. Rowland, S. J. Judge, Visual optics and retinal cone topography in the common marmoset (*Callithrix jacchus*). *Vision Res.* **33**, 1301–1310 (1993).
45. P. M. Daniel, D. Whitteridge, The representation of the visual field on the cerebral cortex in monkeys. *J. Physiol.* **159**, 203–221 (1961).
46. E. L. Schwartz, Anatomical and physiological correlates of visual computation from striate to infero-temporal cortex. *IEEE Trans. Syst. Man Cybern.* **SMC-14**, 257–271 (1984).
47. D. L. Ringach, R. M. Shapley, M. J. Hawken, Orientation selectivity in macaque V1: Diversity and laminar dependence. *J. Neurosci.* **22**, 5639–5651 (2002).

Acknowledgments: We thank G. Goodhill for commenting on an early version of the manuscript, and K. Worthy for assistance in data collection and histology. **Funding:** Funded by research grants from the National Health and Medical Research Council (1083152, 1122220, and 1128755) and Australian Research Council (DP170104600 and CE140100007).
Author contributions: H.-H.Y., M.G.P.R., N.S.C.P., and E.Z. designed the electrophysiology experiments and collected the data. All authors contributed to the data analysis. H.-H.Y. and D.P.R. developed the model. H.-H.Y., E.Z., M.G.P.R., and N.S.C.P. wrote the paper. H.-H.Y. (as employee of IBM), M.G.P.R., and E.Z. revised the manuscript. **Competing interests:** The authors declare that they have no competing interests. **Data and materials availability:** All data needed to evaluate the conclusions in the paper are present in the paper and/or the Supplementary Materials. Additional data related to this paper may be requested from the authors. The source code of the model (implemented in Python using the Tensorflow machine learning library) is available at https://github.com/hsinhaoyu/DM_Retinotopy.

Submitted 15 October 2019
Accepted 9 September 2020
Published 28 October 2020
10.1126/sciadv.aaz8673

Citation: H.-H. Yu, D. P. Rowley, N. S. C. Price, M. G. P. Rosa, E. Zavitz, A twisted visual field map in the primate dorsomedial cortex predicted by topographic continuity. *Sci. Adv.* **6**, eaaz8673 (2020).